International Journal of Thermophysics (2023) 44:173
https://doi.org/10.1007/s10765-023-03281-4

Investigation of the Density Dependence of the Influence Parameter

Eva Mühlegger[1] · **Kai Langenbach**[1]

Received: 30 August 2023 / Accepted: 17 October 2023 / Published online: 10 November 2023

Abstract

In chemical engineering, interfacial properties play an important role in the design of thermal separation units and also in product design. Two important surface properties are the surface tension between fluid phases and the adsorption of fluids on solids. Of the various ways of describing and calculating these properties, density gradient theory (DGT) is by far the least computationally demanding. However, while surface tension is well described by DGT, adsorption is typically not. One possible reason for this is the constant known as the influence parameter of DGT. This parameter has a real physical meaning—it is the second moment of the direct correlation function—and should therefore depend on the density. In this contribution the density dependence of the influence parameter is investigated. Both, the surface tension between liquid and vapor and the adsorption of vapor or gas on solids of the Lennard–Jones truncated and shifted fluid, are calculated and compared with molecular simulation data. A functional form is identified which retains most of the accuracy of the surface tension while greatly improving the description of the adsorption.

Keywords Adsorption · Density gradient theory · Influence parameter · Lennard–Jones fluid · Surface tension

Dedicated to Prof. Dr.-Ing. habil. Roland Span on the occasion of his 60th birthday and in recognition of his great achievements in experimental and theoretical thermodynamics. We thank you for your dedication and remarkable work for the community and for all the great contributions to the field.

Special Issue in Honor of Professor Roland Span's 60th Birthday.

✉ Kai Langenbach
Kai.Langenbach@uibk.ac.at

[1] Department of Chemical Engineering, Universität Innsbruck, Innsbruck, Austria

1 Introduction

Adsorption layers are always formed at the interface when fluids come into contact with solids under real conditions. Especially in high precision measurements of densities, adsorption can lead to significant errors, which have to be accounted for. However, the complex nature of the interfaces present in these measurements is almost only accessible by theoretical means, specifically if mixtures are concerned. To understand their behavior, adsorption calculations are of particular interest in measurement applications, *e.g.*, in fluid density measurement [1, 2]. Tietz *et al.* [1] calculated the adsorption behavior on planar surfaces with molecular dynamics (MD) simulations to describe the adsorption isotherm within the gravimetric experiments.

Adsorption as a unit operation also plays an increasing role in chemical engineering and its measurement and calculation or prediction are becoming increasingly important, *e.g.* [3–16]. Most theoretical methods, however, require a huge computational effort. Therefore, it is interesting to calculate interfacial phenomena such as surface excess and surface tension using simpler methods such as density gradient theory (DGT) [17–20] in order to derive other observable quantities to describe the behavior of fluids for technical applications and product design.

There are several approaches to modeling surface tension γ^*[1] and surface excess Γ^* from empirical equations [21] to MD simulations [13, 22–26]. They differ primarily in the amount of computational resources required. Currently, MD simulations take the largest computational effort. One way to calculate adsorption isotherms is the ideal adsorbed solution theory (IAST) [27]. It assumes that the adsorbed phase behaves like an ideal solution with no interactions between the adsorbed molecules in the adsorbed phase mixture. The real adsorbed solution theory (RAST) [28] gains accuracy but loses predictive character. It incorporates experimental data to estimate the interaction parameter to determine adsorption isotherms. Both models, IAST and RAST, are calculated with low computational demands. To increase the precision of the calculation, classical density functional theory (DFT) [29] is able to calculate interfacial properties, like surface tension and adsorption isotherms [14, 30–32] with an increase in computational effort. In DFT, Helmholtz' energy is expressed as a non-local—and thereby computationally expensive—functional of the density profiles of the constituent molecules. A simplified and considerably faster method compared to DFT is DGT. DGT in engineering has been in use for many years for surface tension calculations of pure substances and mixtures, *e.g.* [17, 24, 33–40]. In vapor-liquid-equilibrium (VLE), DGT models surface tension in a promising way and with low computational effort for pure substances and mixtures [34, 37, 38, 41–44].

Currently, there is no sufficient model to describe both, surface tension and adsorption with the DGT with one set of parameters. This contribution aims to calculate the adsorption behavior also with DGT.

[1] All variables marked with an asterisk are in reduced units.

In DGT, mostly a constant influence parameter κ^*, adjusted to the investigated substances, is used for surface tension calculations so far, e.g. [17, 36–39, 45]. For solid–fluid interactions there is the concept of fitting the influence parameter to adsorption isotherms [46]. Rehner *et al.* [40] proposed a local density and temperature-dependent influence parameter for predictive DGT. Their approach is based on DFT and weighted densities and is limited to fluid-liquid interfaces. To describe adsorption with DGT, Butz [16, 47] stated that a fitted influence parameter improves the prediction of adsorption isotherms. Depending on the number of carbon atoms and surface energies, the influence parameter for surface tension calculations is lowered by a factor of ten to describe gas adsorption. We propose a different approach with a density dependent influence parameter, where the same influence parameter is used to describe surface tension and adsorption.

In this contribution, the adsorption between fluids and solids, as well as the surface tension between vapor and liquid phases are studied using DGT. For this purpose, a density dependent influence parameter is used to improve the calculation results. A second order polynomial approach is chosen, whose individual parameters are varied. The differently optimized parameter combinations are obtained by selecting the non-dominated points in the objective function space. The results are further compared to already known MD data from Vrabec *et al.* [48] and Liu *et al.* [12]. To do so, DGT must use a good equation of state. There are different EOS that describe a LJTS potential, *e.g.* [49, 50]. This work is based on the perturbated truncated and shifted equation of state (PeTS-EOS) from Heier *et al.* [50], because it can describe all desired properties with high accuracy and is valid in the interface. Other EOS, *e.g.*, PC-SAFT [51] could be used instead for real fluids.

Results are shown for surface tension at different temperatures and adsorption at different wall potentials at multiple surface energies.

2 Methods and Models

2.1 Equation of State

The PeTS-EOS [50] is used as equation of state (EOS) because it accurately represents the Lennard–Jones truncated and shifted (LJTS) fluid. It shows physical behavior in unstable regions within the spinodal and—as most modern EOS—is also suitable for supercritical states that are also investigated in this work [50]. The modeled interactions are based on a Lennard–Jones potential (LJ). In MD, the potential is often modified to a LJTS potential to reduce the number of interactions between the molecules. The critical temperature of the LJTS fluid with a cut-off radius of $r^*_{cut-off} = 2.5$, modeled with PeTS-EOS as it is used in this work, is $T^*_c = 1.0779$, the critical density is $c^*_c = 0.3190$. All thermodynamic properties of the fluid, such as the free energy density Φ^*, the chemical potential μ^* and the pressure p^* are derived from the free energy per particle. For further information, the interested reader is referred to [50].

The density of the fluid adsorbed to a wall can largely increase in comparison to the bulk density. The PeTS-EOS is based on a hard sphere reference. If the density increases, also the packing fraction η increases, until a singularity in the EOS is reached, where the equation of state cannot be solved anymore. Therefore, the model is limited by a maximum density, where the packing fractions is still $\eta < 1$. Also, the expected density increase in the adsorbate layer is limited by the packing fraction.

2.2 Density Gradient Theory

Density gradient theory (DGT) is the simplest, qualitatively correct molecular model for describing interfaces [52]. The theory is mostly based on the early work of van der Waals [53] and the work of Cahn and Hilliard [54], who reformulated the theory [17–20].

The phase transition along a one-dimensional interface, characterized by the coordinate normal to the interface z^*, exhibits a density gradient. The free energy functional $F^*[c^*(z^*)](T^*)$ of the phase transition is developed around the homogenous state of the energy density Φ_0^* from a Taylor series truncated after the second term. When the temperature dependence of the free energy and of the density is neglected, the following functional dependence is obtained [17, 54]:

$$F^*\left[(c^*(z^*))\right] = \int_V \Phi_0^*(c^*(z^*)) + \frac{1}{2}\kappa^*|\nabla c^*|^2 dV \tag{1}$$

The free energy density of the homogenous state Φ_0^* is calculated using the selected equation of state. The second term of Eq. 1 represents the resistance to changes in density which is scaled by κ^*. Usually, the so-called influence parameter κ^* is taken as constant. However, it is known [17, 18, 33] that it represents the second moment of the direct correlation function, which depends on both, the local density and the density profile. Following the general idea of a Taylor series expansion, κ^* should not depend on ∇c^* or $|\nabla c^*|^2$, however, it may depend on temperature T^* and density c^*. Here, it is assumed that it is only dependent on c^* to allow a better representation of gas phase adsorption. This assumption is somewhat arbitrary and can be seen as a starting point for further investigations.

In a μVT system, both phases at the VLE phase boundary have the same pressure, temperature, and chemical potential. The chemical potential is obtained by functional minimization of the free energy with respect to $c^*(z^*)$:

$$\mu^* = \frac{\delta F^*[c^*(z^*)]}{\delta c^*} = \mu_0^*(c^*(z^*)) + \frac{1}{2}\frac{\partial \kappa(c^*)}{\partial c^*}|\nabla c^*|^2 - \nabla\kappa^*(c^*)\nabla c^* - \kappa^*(c^*)\nabla^2 c^* \tag{2}$$

To meet the constraints of the VLE, the chemical potential is set as boundary condition, therefore it needs to be constant and have the according bulk value of either phase. For adsorption calculation, a solid phase is introduced to the system

by adding an external potential U^*_{ext}, Eq. 3.[2] The solution of Eq. 3 is the density profile $c^*(z^*)$ along the phase boundary, which is further used to determine the surface tension γ^* in case of VLE and the surface excess Γ^* in case of adsorption. Further information on the numerical methods is shown in Appendix A. After some algebra, the resulting set of equations is

$$\mu^*(c^*(z^*)) - \frac{1}{2}\frac{\partial\kappa(c^*)}{\partial c^*}|\nabla c^*|^2 - \kappa^*\nabla^2 c^*(z^*) - \mu^*_{bulk} + U^*_{ext} = 0 \tag{3}$$

$$\gamma^* = \int_{c^{*v}}^{c^{*l}} \sqrt{2\kappa^*\Delta\omega}dc^* \tag{4}$$

$$\Delta\omega = \Phi_0 - c^*\mu^{*eq} + p^{*eq} \tag{5}$$

$$\Gamma^* = \int_{z_0^*}^{z_1^*} \left[c_f^*(z^*) - c_f^{*b}\right]dz^* \tag{6}$$

For the surface tension calculation, Eq. 4, the integral limits are the bulk densities, c^{*v} of the vapor and c^{*l} the liquid phase. The surface excess, Eq. 6, is the integral of the density between z_0^*, which is the first intersection of the density profile with the bulk density and ends at z_1^*, when the final bulk density is reached.

To investigate various solid phases, the following parameters for the external potential U^*_{ext} are used [12, 55]:

$$U^*_{LJ-10-4-3}(z^*) = 2\pi\varepsilon^*_{sf}\rho^*_s\sigma^{*2}_{sf}\Delta\left(\frac{2}{5}\frac{\sigma^{*10}_{sf}}{z^{*10}} - \frac{\sigma^{*4}_{sf}}{z^{*4}} - \frac{\sigma^{*4}_{sf}}{3\Delta(z^* + 0.61\Delta)^3}\right) \tag{7}$$

$$U^*_{LJ-9-3}(z^*) = \frac{4}{3}\pi\varepsilon^*_{sf}\rho^*_s\sigma^{*3}_{sf}\left(\frac{\sigma^{*9}_{sf}}{z^{*9}} - \frac{\sigma^{*3}_{sf}}{2z^{*3}}\right) \tag{8}$$

The different types are the 10–4–3, Eq. 7, and the 9–3, Eq. 8, potential. The solid, represented by a wall potential is located at $z^* = 4.75$. For details on the potentials, the reader is referred to Liu *et al.* [12]. The LJTS potential used is given by the following Eq. 9, with a cut-off radius of $z^*_c = 2.5$.

$$U^*_{LJTS}(z^*) = U^*_{LJ}(z^*) - U^*_{LJ}\left(z^*_c\right) \tag{9}$$

The fluid, solid, and solid–fluid size parameters of the external potential equal $\sigma^*_f = 1$, $\sigma^*_s = 1$, and $\sigma^*_{sf} = 1$, as well as the energy parameter of the fluid, $\varepsilon^*_f = 1$. The solid density is $\rho^*_s = 1.07$ and the spacing between planes in the solid lattice is $\Delta = 0.775$. The solid–fluid energy parameter ε^*_{sf} is varied between 0.3 and 2.0 and

[2] Compared to Eq. 13 of Liu et al. [12], the sign of the potential is corrected here.

Table 1 Investigated cases for the adsorption calculation, with different types of the potential, two different temperatures and up to four different surface energies

Wall potential	T^*/T_c^*	ε_{sf}^*
LJTS 10–4–3	0.8	0.3
		0.514
		0.75
		2.0
LJTS 10–4–3	1.1	0.514
LJ 10–4–3	0.8	0.514
LJTS 9–3	0.8	0.514
LJ 9–3	0.8	0.514

the different parameters for the external potential are listed in Table 1. These correspond to the parameters from Liu *et al.* [12].

2.3 Influence Parameter

The influence parameter κ^* contains the information about the structure of the phase transition and essentially determines the response of the DGT to the local derivative of density [17]. Physically, the influence parameter is associated with the second moment of the direct correlation function [17, 18, 33].

So far, the influence parameter κ^* is mostly described as a constant. Although the dependence of the influence parameter on the density is not denied, it is described as very small and neglectable [17], based on [56, 57], where it is stated, that for low densities, the influence parameter is independent of the density. During adsorption of the fluid on the solid, an increase in fluid density is found at the wall, the so-called surface excess. Since one can no longer assume very low densities, the density dependence of the influence parameter must be considered. Heier *et al.* [50] were able to show that the temperature dependence of the influence parameter is neglectable for the LJTS fluid, if the density dependence is neglected, too. We assume here that the temperature dependence can also be neglected for a density dependent influence parameter, but this is somewhat arbitrary. Heier *et al.* [50] derived the constant influence parameter from surface tension data up to the critical temperature, obtaining

$$\kappa^* = 2.7334 \tag{10}$$

In this contribution, a density dependent expression for the influence parameter is used. For simplicity, a second order polynomial is chosen. This is a compromise between keeping the density dependency on a low mathematical level, but improving the adsorption model significantly.

$$\kappa^*(c^*) = A + Bc^* + Cc^{*2} \tag{11}$$

The parameter A is chosen to be zero here, while B and C are fitted in this contribution. This choice is not rigorous, since the influence parameter is formally linked

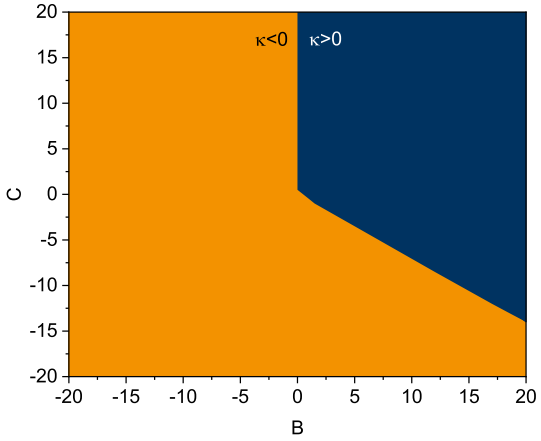

Fig. 1 Possible parameter sets for C and B for the density dependent influence parameter are shown as blue (dark) area. According to the selected constrains, the influence parameter has to be positive across the density range and zero at zero density (Color figure online)

to the direct correlation function [17, 18, 33], but leads to a lower numerical effort needed to fit the remaining parameters.

3 Results

The results section is divided into three parts, namely, the optimization of the parameters set for the density dependent influence parameter, the surface tension, and the adsorption. The results of the DGT data using a density dependent approach for the influence parameter are compared to the MD data. All adsorbed fluid data corresponds to gas phase adsorption.

3.1 Estimation of Pareto Optimal Parameter Sets

The second order polynomial of the density dependent influence parameter is optimized to find a set of parameters that can describe adsorption behavior and surface tension phenomena. Therefore, the concept of a pareto front is used, following Stöbener *et al.* [58], to find the non-dominated points. These are parameter sets that cannot be improved in one property, without decreasing in the other property, *i.e.*, the best compromises.

The parameters A, B, C of Eq. 11 are constrained as follows: At zero density, the influence parameter is also set to zero, therefore the parameter A vanishes. For reasons of physical correctness, a further condition is imposed, namely that the influence parameter itself is always positive in the range from zero to a maximum density of a closed packed structure of c^*_{max}. The temperature dependence of the diameter is neglected. These constrains restrict the range of the parameters B and C to the blue (dark, color online) area in Fig. 1.

A coarse grid is placed over the remaining parameter space containing natural numbers and one number at 0.5 in between as possible parameters. This results in a maximum range of $[-14, 20]$ for the C parameter and $[0, 20]$ for the B parameter.

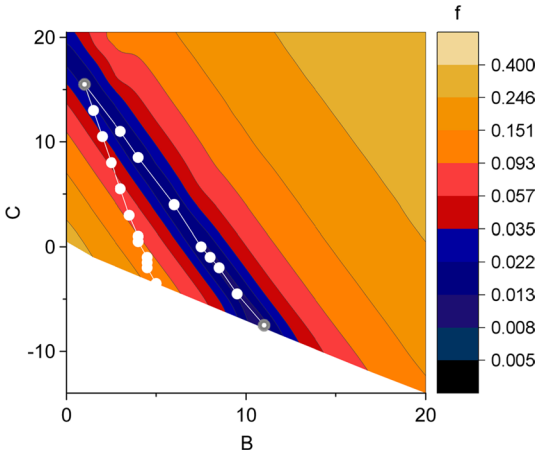

Fig. 2 Surface tension deviation in the parameter space. The darker area corresponds to smaller deviation. The non-dominated points are plotted as white filled circles. The two further investigated non-dominated points are additionally marked with gray circles (Color figure online)

For all parameter sets, the surface tension γ^* and the surface excess Γ^* are calculated and the deviations f_{γ^*,Γ^*} to the MD data are determined according to Eqs. 12 and 13, respectively.

$$f_{\gamma^*} = \sqrt{\frac{1}{N_{\gamma^*}} \sum_{i=1}^{N_{\gamma^*}} \left(x_{i,DGT} - x_{i,MD}\right)^2} \tag{12}$$

$$f_{\Gamma_i^*} = \sqrt{\frac{1}{N_{\Gamma_i^*}} \sum_{i=1}^{N_{\Gamma_i^*}} \left(x_{i,DGT} - x_{i,MD}\right)^2} \tag{13}$$

$x_{i,DGT}$ is the result of the surface tension γ^* or surface excess Γ^*, respectively, calculated with DGT, at the investigated temperature or adsorption setting i, $x_{i,MD}$ is the corresponding result of the MD data from the literature [12, 48]. Here, N_{γ^*,Γ_i^*} is the size of the data set being compared, *e.g.*, for the surface tension, there are nine different temperatures, $N_{\gamma^*} = 9$. For the adsorption calculation, $N_{\Gamma_i^*}$ varies due to the number of investigated bulk densities at different temperatures, surface energies and wall potentials (the details of the adsorption settings are shown in Appendix C). To obtain only one value for one parameter set, Eq. 14 is used to combine the eight different adsorption settings, therefore, $N_{\Gamma^*} = 8$ in Eq. 14.

$$f_{\Gamma^*,total} = \sqrt{\frac{1}{N_{\Gamma^*}} \sum_{i=1}^{N_{\Gamma^*}} f_{\Gamma_i^*}^2} \tag{14}$$

All parameter combinations of B and C are investigated to find the non-dominated points with the smallest possible deviation between DGT and MD. The

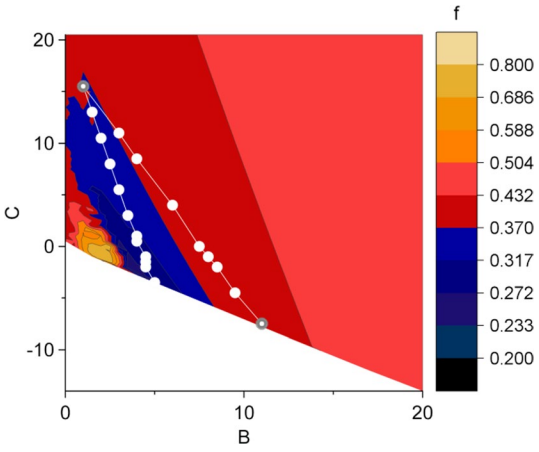

Fig. 3 Surface excess deviation in the parameter space. The darker area corresponds to smaller deviation. The non-dominated points are plotted as white filled circles. The two further investigated non-dominated points are additionally marked with gray circles (Color figure online)

results are depicted as contour plots in the parameter space in Figs. 2 and 3. The two parameter combinations of the non-dominated points studied in more detail are marked with gray circles.

The blue (dark) color stands for a small deviation or the best parameter combinations, the most unfavorable ones are in the orange (light-colored) area.

Figure 2 represents the results for the surface tension. The color reflects the root mean square deviation calculated with Eqs. 12–14 to corresponding MD data from Liu *et al.* [12]. It shows an optimum in form of a valley across the parameter space (blue, dark color), starting from the lowest region in the center at negative C values up to the top left corner.

The adsorption deviation is plotted in Fig. 3, where the minimum deviation (dark blue) is near $B = 4.0, C = -2.0$. Compared to the surface tension data, the region of low f-values of the parameter combinations is very small.

While the deviation defined by Eqs. 11–13 is suitable for optimization, we define the absolute relative deviation (ARD) by

$$f_{\gamma^*,ARD} = \sqrt{\frac{1}{N_{\gamma^*}} \sum_{i=1}^{N_{\gamma^*}} \frac{|x_{\gamma^*,DGT} - x_{\gamma^*,MD}|^2}{x^2_{\gamma^*,MD}}} \tag{15}$$

$$f_{\Gamma_i^*,ARD} = \sqrt{\frac{1}{N_{\Gamma_i^*}} \sum_{i=1}^{N_{\Gamma_i^*}} \frac{|x_{\Gamma_i^*,DGT} - x_{\Gamma_i^*,MD}|^2}{x^2_{\Gamma_i^*,MD}}} \tag{16}$$

$$f_{\Gamma^*_{total},ARD} = \sqrt{\frac{1}{N_{\Gamma^*}} \sum_{i=1}^{N_{\Gamma^*}} f^2_{\Gamma^*,ARD}} \tag{17}$$

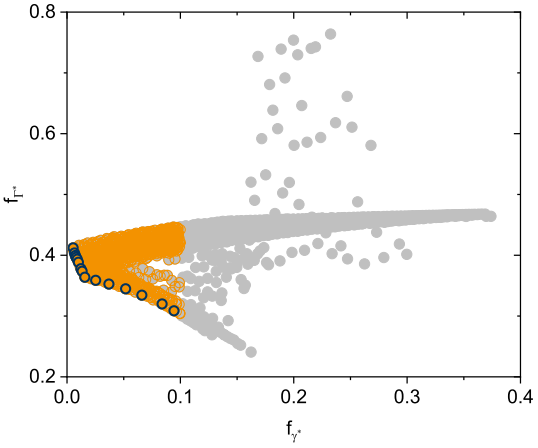

Fig. 4 For each investigated parameter set for the density dependent influence parameter the deviation of the adsorption calculations is plotted over the deviation of the surface tension in the objective function space as gray filled circle. The orange circles represent deviation within the limit of $f_{\gamma^*} < 0.1$. The non-dominated points are marked with thicker, blue circles (Color figure online)

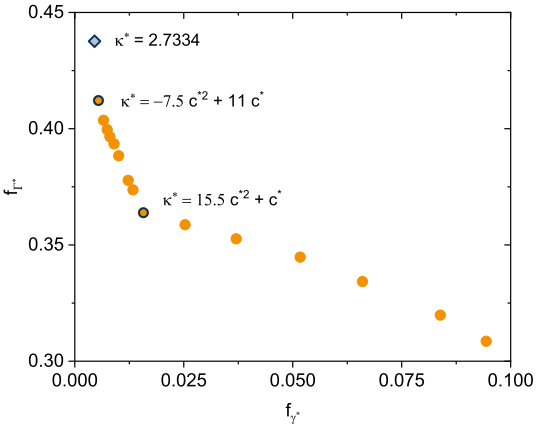

Fig. 5 The non-dominated points in the objective function space. The two further investigated parameter sets, C = − 7.5, B = 11.0 and C = 15.5, B = 1.0 are dark circled. The constant influence parameter is shown as gray diamond (Color figure online)

in order to compare both results. The overall level of absolute relative deviation is much higher for the adsorption results, with a minimum of $f_{\Gamma^*,ARD} \sim 0.38$, while the surface tension results are $f_{\gamma^*,ARD} \sim 0.03$.

The very well-defined optimum surface tension valley has an intersection at an acceptably low level of adsorption deviation at $B = 1.0, C = 15.5$. To approach the best combinations, the deviations are plotted in the objective function space, Fig. 4. The surface tension results are on the x-axis and the adsorption results on the y-axis. The ideal parameter combination should lead to a point close to the origin of the coordinates that has the lowest deviation in both, surface tension and adsorption.

In order to maintain a high level of accuracy in the surface tension calculations, an arbitrary limit is set at a deviation of $f_{\gamma^*} = 0.1$. This is shown in Fig. 4, where only the orange (light-colored) parameter sets are further considered. The non-dominated points are selected manually, and highlighted by rings around the circles in Fig. 4. They are additionally depicted in Fig. 5, when the approximation to the pareto front is shown.

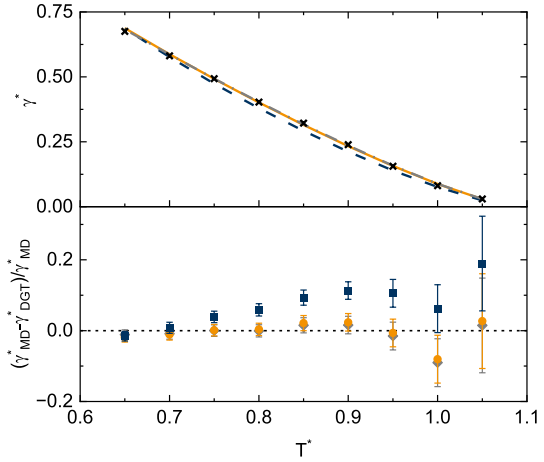

Fig. 6 In the upper half, the surface tension calculated with MD (black markers) and DGT (lines) is shown. The constant influence parameter is plotted as a gray dash-dotted line, parameter set α as orange, line and β as blue, dashed line. In the lower half, the deviation of the DGT in comparison to the MD data from [48] (dotted zero line) is shown at different temperatures of the two further investigated density dependent influence parameter (α as orange circles, β as blue squares and the constant influence parameter as gray diamonds) (Color figure online)

The deviation from the MD data [12, 48] calculated with the constant influence parameter is depicted as a diamond in Fig. 5. It has a larger deviation for adsorption but at the same time the lowest for surface tension. The constant influence parameter is also an optimized parameter combination since it is part of the non-dominated points in the objective function space.

Two parameter combinations of the obtained non-dominated points are further studied. They are marked with the blue circles in Fig. 5. The combination that shows the highest accuracy in surface tension and an increase of accuracy in adsorption is Eq. 18. This is further referred to as parameter set α.

$$\kappa^* = -7.5c^{*2} + 11c^* \tag{18}$$

In terms of surface tension, this set of parameters represents the optimal area in Fig. 2. It is perfectly situated in the middle of the valley, moreover in the deepest spot. In contrast, these parameters do not ideally reflect the adsorption. It is far outside the ideal area in Fig. 3.

The parameters of Eq. 19 are chosen, as they show low deviation in both, surface tension and adsorption and correspond to the intersection of the optimal areas in Figs. 2 and 3. This is also the inflection point of the non-dominated points in the objective function space (Fig. 5). It is further referred to as parameter set β.

$$\kappa^* = 15.5c^{*2} + c^* \tag{19}$$

This parameter set shows better results for adsorption. Parameter set β is the last one on the pareto front with an average deviation of γ^* below 2.5 %. Although

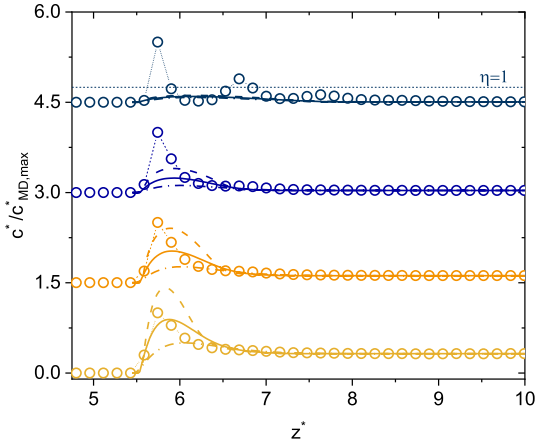

Fig. 7 Normalized density profiles of the adsorption at $T^*/T_c^* = 0.8$. The solid is described by a LJTS potential. The MD data are plotted as circles, with dotted lines as a guide to the eye, the constant influence parameter as dash-dotted line and the density dependent influence parameter sets α as line and β as dashed line. The lowest surface energy $\varepsilon_{sf}^* = 0.514$ represented by the yellow plots at $c_{bulk}^* = 0.0226$, which are multiplied by 2.5. The surface energy of $\varepsilon_{sf}^* = 0.514$ at $c_{bulk}^* = 0.02157$ are the orange ones, the blue plots correspond to $\varepsilon_{sf}^* = 0.75$ at a bulk density of $c_{bulk}^* = 0.01887$, and the dark blue one are multiplied with 0.25 at a surface energy of $\varepsilon_{sf}^* = 2.0$ with a bulk density of $c_{bulk}^* = 0.0239$. The data are shifted by 0.0, 1.5, 3.0, 4.5, respectively (Color figure online)

there are many further possible optimized parameter sets, with better results in adsorption, the ability to calculate surface tension should not be lost, therefore no other parameter sets are further investigated in this contribution. The cut-off at the deviation of 2.5 % is chosen somewhat arbitrarily, as all solutions on the Pareto front are optimal. It roughly corresponds to an uncertainty of 1 mJ•m^{-2} for real substances in a medium surface tension range.

3.2 Surface Tension

In Fig. 6, the surface tension results are plotted in the upper part, with the MD data as black markers, the constant influence parameter as gray dash-dotted line, the parameter set α as orange line and β as dashed blue line. Additionally, the relative deviation from the MD data are shown in the lower part, with the parameter set α as orange dots, the parameter set β as blue squares. Also, the deviation in surface tension of the constant influence parameter is depicted as diamonds to compare the achieved level of accuracy. The deviation of DGT data originates from the MD data, otherwise the DGT data would not show any error bars. The detailed surface tension results are shown in Appendix B.

The constant influence parameter originates from surface tension data only [50], therefore these results are difficult to surpass with another approach for the influence parameter. However, the parameter set α (orange, light color, circles) shows, as to be expected from Fig. 5, the same behavior as the constant influence parameter with

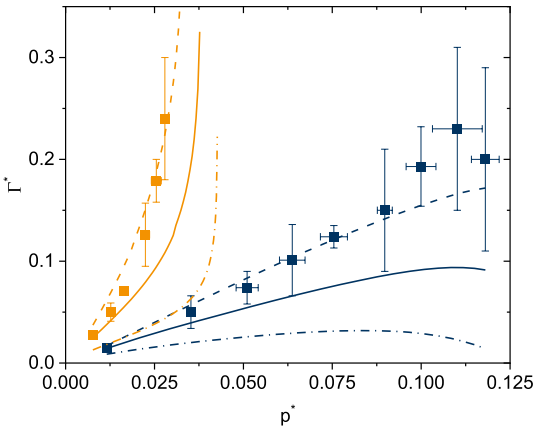

Fig. 8 Adsorption isotherms of the LJTS 10–4–3 potential with $\varepsilon^*_{sf} = 0.514$ at $T^*/T^*_c = 0.8$ (orange) in comparison to $T^*/T^*_c = 1.1$ (blue). The MD data are plotted as squares, the constant influence parameter as dash-dotted line, the parameter set α as line and β as dashed line (Color figure online)

only small deviations from the MD data in Fig. 6. The zero line in the lower part is mostly within the error bars at all temperatures. The deviation is very small (< 5 %), except at $T^* = 1.0$. The parameter set β is shown in blue (dark color, squares). Overall, it shows a higher deviation from the MD data. At low temperatures, the surface tension is similar to the MD data, but already at $T^* = 0.75$ the parameter set β shows significantly lower surface tension results. The deviation of the parameter set β increases significantly up to 10 %. At the highest temperature, $T^* = 1.05$, the surface tension result of parameter set β even deviates up to 20 %, however, the absolute error at this temperature is only $\Delta\gamma^*_{T^*=1.05} = 0.006$. The density profiles are shown in Appendix D.

3.3 Adsorption

Figure 7 exemplarily shows the normalized density profiles. They are normalized by dividing the density by the maximum density of the MD data of each potential and shifted for better display. The profiles calculated with MD (circles), with DGT with the constant influence parameter[3] (dash-dotted line) and DGT with a density dependent influence parameter, A (line) and B (dashed) for the LJTS 10–4–3 wall potential at $T^*/T^*_c = 0.8$ with $\varepsilon^*_{sf} = 0.3$ (yellow), $\varepsilon^*_{sf} = 0.514$ (orange), $\varepsilon^*_{sf} = 0.75$ (blue) and $\varepsilon^*_{sf} = 2.0$ (dark blue). The bulk densities are all around $c^*_{bulk} \sim 0.02$.

In general, DGT with a constant influence parameter underestimates adsorption. Close to the solid, there is first neither a sharp nor a rapid increase of the fluid density but a slow rise with a very slow decay afterwards. For all conditions studied, the DGT with a constant influence parameter calculates much lower values for the surface excess than with a density dependent influence parameter. The adsorption profiles obtained from the density dependent influence parameter show larger and broader increases in surface excess, but always only one peak, as is to be expected. The peak height is limited by the hard sphere reference of the EOS, *i.e.*, the packing

[3] Recalculated here with the correct sign of the solid–fluid potential in Eq. 3.

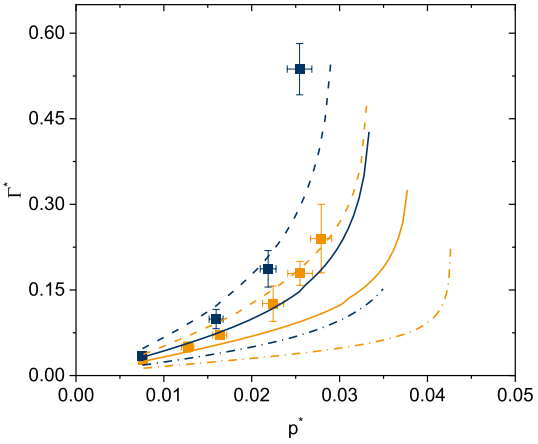

Fig. 9 Adsorption isotherms of the LJTS 10–4–3 potential (orange) in comparison to the LJ-10–4–3 potential (blue) at $T^*/T_c^* = 0.8$ with $\varepsilon_{sf}^* = 0.514$. The MD data are plotted as squares, the constant influence parameter as dash-dotted line, parameter set α as line, and β as dashed line (Color figure online)

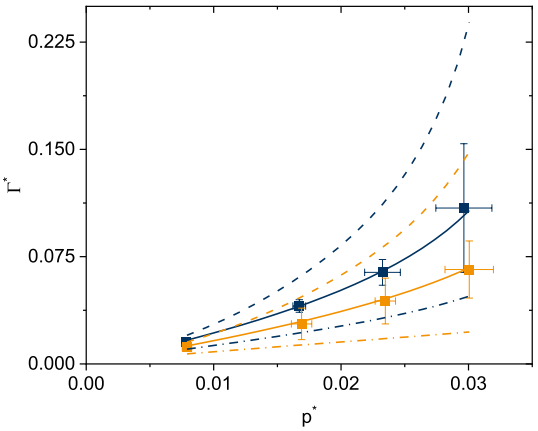

Fig. 10 Adsorption isotherms of the LJTS 9–3 potential (orange) in comparison to the LJ-9–3 potential (blue) at $T^*/T_c^* = 0.8$ with $\varepsilon_{sf}^* = 0.514$. The MD data are plotted as squares, the constant influence parameter as dash-dotted line, the parameter set α as line and β as dashed line (Color figure online)

fraction η cannot be greater than one. This is illustrated by the dotted line in Fig. 7 for $\varepsilon_{sf}^* = 2.0$., where the MD data show packing fractions larger than 1.

In the MD data, only one peak is generally found in the adsorption profiles at low fluid bulk densities, which increases at higher densities. This describes the presence of a monolayer, while a further increase in density results in multilayer formation. Moreover, at larger fluid densities a second or even third peak occurs in the MD data. This reflects the different behaviors of gas phases interacting with a surface, where further aggregation might take place at the adsorbate layer itself.

All the DGT data in Fig. 7 exhibit an increase of density near the wall, the extent of which depends on the bulk density. Despite the difference of the overall shape between the DGT and MD, the total surface excess looks similar as the best DGT curves appear to represent the sum of all peaks.

The more informative representation of the adsorption results are the adsorption isotherms. The isotherms result from the other investigated bulk densities, temperatures, and wall potentials. The solid lines correspond to the density

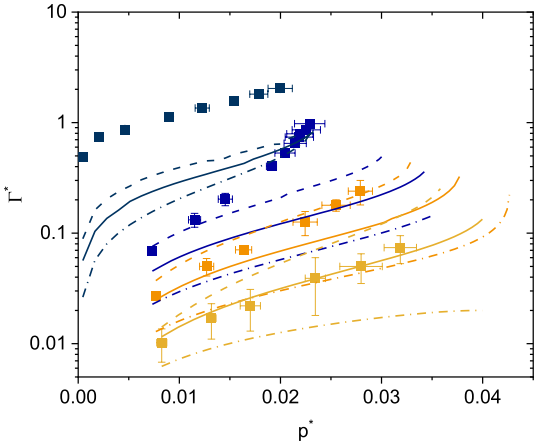

Fig. 11 Adsorption isotherms of the LJTS 10–4–3 potential at $T^*/T_c^* = 0.8$ and different surface energies, $\epsilon_{sf}^* = 0.3$ (yellow), $\epsilon_{sf}^* = 0.514$ (orange), $\epsilon_{sf}^* = 0.75$ (blue) and $\epsilon_{sf}^* = 2.0$ (dark blue). The MD data are plotted as squares, the constant influence parameter as dash-dotted line, the parameter set α as line and β as dashed line (Color figure online)

dependent parameter set α, the dashed lines represent the parameter set β and the dash-dotted line the constant influence parameter, the square markers the MD data. Different comparisons of the isotherms are shown Figs. 8, 9, and 10.

Figure 8 depicts the adsorption isotherms of the LJTS potential with $\epsilon_{sf}^* = 0.514$ at different temperatures, one smaller than the critical temperature, one higher.

Using the density dependent influence parameter results in a huge increase in precision compared to the constant one (dash-dotted lines). At $T^*/T_c^* = 0.8$, all isotherms, the MD data, the constant influence parameter and the density dependent influence parameter show the same curvature. The curvature of the MD data for $T^*/T_c^* = 1.1$ is unclear due to large error bars. While it may look more likely than not that there is a wetting transition in between the two temperatures, which would result in a change of curvature, the data are not fully conclusive. If there is indeed a wetting transition and taken together with the good result for surface tension over the whole temperature range, the temperature independence of κ^* seems likely to be a good approximation. However, since the data are not conclusive, no definite answer can be given with regard to this. Over the entire pressure range, the parameter set β is a better representation of the MD data, but at low pressures, the parameter set α is a more accurate calculation of the surface excess.

In Figs. 9 and 10 the adsorption isotherms for different potential types are shown, LJ/LJTS 10–4–3 and LJ/LJTS 9–3, respectively.

While in Fig. 9, the adsorption isotherms are both best described by the parameter set β of the density dependent influence parameter, in Fig. 10 the MD data are best described by the parameter set α. Common to both is that the constant influence parameter again reflects the adsorption poorly. Fig. 11 compares the adsorption isotherms of the LJTS 10–4–3 potential at different surface energies at $T^*/T_c^* = 0.8$. The surface excess is plotted on a logarithmic scale.

The parameter set α (line) can calculate the lowest surface energy of $\epsilon_{sf}^* = 0.3$ with acceptable accuracy, also the lower two pressures for $\epsilon_{sf}^* = 0.514$. At greater surface energies, it underestimates the surface excess. With the parameter set β, the adsorption isotherms at low surface energies are slightly overestimated, but can be computed up

to $\varepsilon_{sf}^{*} = 0.75$ at low pressures. None of the investigated density dependent influence parameter sets can correctly calculate the adsorption isotherms at $\varepsilon_{sf}^{*} = 2.0$. Although the qualitative shape of the isotherm is similar, the surface excess is always underestimated with DGT. Again, the constant influence parameter reflects the adsorption very poorly, as all dash-dotted curves are at far lower surface excess values.

4 Conclusions

The aim of this contribution is to modify the influence parameter of the DGT, to calculate both, surface tension between fluids and adsorption between gases and solids with the same model. To optimize $\kappa^{*}(c^{*})$ the parameters of the second order polynomial density relation of the influence parameter are systematically varied, obtaining non-dominated points. The constant influence parameter is also part of them, with the lowest deviation in surface tension and the highest in adsorption. Two sets of optimized parameters are examined in more detail in comparison to the constant influence parameter and the MD data from Liu *et al.* [12] and Vrabec *et al.* [48] in terms of adsorption and surface tension.

Calculation of surface tension data with the same degree of accuracy as the constant influence parameter is possible, especially with the parameter set α. Increased accuracies in adsorption are reached with the density dependent influence parameter. It is shown that DGT with PeTS-EOS [50] cannot calculate the adsorption data for higher surface energies, because it is limited by the largest hard sphere packing fraction in the local hard sphere term. Therefore, the application of the DGT is also limited to small surface energies, $\varepsilon_{sf}^{*} = 0.3$ and $\varepsilon_{sf}^{*} = 0.514$.

The parameter set α, $\kappa^{*} = -7.5c^{*2} + 11.0c^{*}$, reaches nearly the same precision in surface tension as the constant influence parameter. The accuracy of adsorption calculations is increased, therefore, especially at low pressures and for the low surface energies, this density dependent influence parameter set should be used.

The obtained density dependent relation of the influence parameter has advantages over previously known constant values, as it is possible now, to calculate both, surface tension and adsorption, with the same expression for the influence parameter. DGT with a density dependent influence parameter is a competitive method to compute adsorption isotherms and surface tension, since the computational effort is low and the calculations are very fast. The accuracy of the calculation is highly increased, especially for the adsorption.

Appendix A: Numerical Methods

To calculate surface tension, Eq. 2 is solved to obtain the density profile. It contains the first and second derivative of the density with respect to space. They are approximated by finite differences.

For all adsorption calculations and surface tension with temperatures above 0.8, the points are set equidistant. The gradient is expressed by central differences, Eq. 20, the boundary values are forward (Eq. 21), backward (Eq. 22) differences, respectively.

$$\nabla^c c^* \cong \frac{c^*_{i+1} - c^*_{i-1}}{2\Delta z^*_i} \tag{20}$$

$$\nabla^f c^* \cong \frac{c^*_{i+1} - c^*_i}{\Delta z^*_i} \tag{21}$$

$$\nabla^b c^* \cong \frac{c^*_i - c^*_{i-1}}{\Delta z^*_i} \tag{22}$$

The second derivative is approximated according to Eq. 23. The boundaries are treated as explicit values, which correspond to the equilibrium densities of the phases.

$$\nabla^2 c^* \cong \frac{c^*_{i+1} - 2c^*_i + c^*_{i-1}}{\Delta z^{*2}_i} \tag{23}$$

At lower temperatures, the distance between the points is non-equidistantly refined. Therefore, the finite difference method is changed to Eqs. 24 and 25.

$$\nabla c^* \cong \frac{c^*_{i+1} - c^*_{i-1}}{\Delta z^*_i + \Delta z^*_{i-1}} \tag{24}$$

$$\nabla^2 c^* \cong \frac{c^*_{i+1} - c^*_i}{\frac{1}{2}\left(\Delta z^{*2}_i + \Delta z^*_i \cdot \Delta z^*_{i-1}\right)} - \frac{c^*_i - c^*_{i-1}}{\frac{1}{2}\left(\Delta z^*_i \cdot \Delta z^*_{i-1} + \Delta z^{*2}_{i-1}\right)} \tag{25}$$

Convergence problems occurred especially at the phase transition starting from the gas phase of the density profile. This is solved with a smaller Δz^*, therefore non-equidistant data points are set between $-2.5 < z^* < 2.5$. The transition of the refinement is smoothed by reducing the spatial axis in several z-steps in order not to create artificial jumps in the density profile.

Equation 3 is calculated with a trust-region solver, based on the work of Powell [59]. As the finite difference method forms sparse matrices, a trust-region algorithm is applied. It can solve a system of equations in the form of $F_i(x)=0$. The algorithm approximates the function with a simpler form that adequately reflects the behavior in a neighborhood (also known as trust region) around the current point. Then a trial step is performed and the function is evaluated. If an improvement is achieved, the new solution is accepted, otherwise the trust region area around the current point shrinks and the trial step is repeated.

Table 2 Surface tension results for the VLE concentrations with different influence parameters

$T*$	c_l^*	c_v^*	γ_{const}^*	γ_α^*	γ_β^*
0.65	0.8137	0.0040	0.6825	0.6877	0.6857
0.7	0.7870	0.0074	0.5860	0.5874	0.5763
0.75	0.7594	0.0124	0.4929	0.4923	0.4738
0.8	0.7303	0.0198	0.4032	0.4015	0.3793
0.85	0.6988	0.0302	0.3171	0.3151	0.2920
0.9	0.6635	0.0449	0.2352	0.2334	0.2119
0.95	0.6222	0.0659	0.1584	0.1570	0.1395
1	0.5701	0.0972	0.0883	0.0875	0.0760
1.05	0.4927	0.1515	0.0296	0.0292	0.0243

Calculated with $\kappa_{const}^* = 2.7334$ $\kappa_\alpha^* = -7.5c^{*2} + 11.0c^*$ $\kappa_\beta^* = 15.5c^{*2} + c^*$

Appendix B: Surface Tension Results

The surface tension results are shown in Table 2. The liquid and vapor density result from the VLE, the surface tension is calculated following Eq. 4 with the constant influence parameter, the parameter set α, and β.

Appendix C: Surface Excess Results

The adsorption results are shown in Table 3. The temperature, the potential type, the surface energies, and bulk densities are taken from the MD data of [12]. The pressure is calculated with the EOS, the surface excess from the density profile of the DGT according to Eq. 6 with the constant influence parameter and the parameter sets A and B.

Appendix D: Adsorption Profiles

The additional adsorption profiles for the different surface energies of the LJTS 10–4–3 wall potentials are shown in Figs. 12, 13, 14, 15, 16, 17, 18, and 19. The MD data from Liu *et al.* [12] is plotted as circles with dotted lines. Results for the constant influence parameter are depicted as dash-dotted lines. The adsorption profiles for the density dependent influence parameter are divided between the figures for each of the two further investigated parameter sets, each shown as lines in the respective figure.

Generally, the constant influence parameter does not represent any density profile of the MD data well. The approach with a density dependent influence parameter always shows an immediate improvement. For $\varepsilon_{sf}^* = 0.3$ the adsorption profiles are

Table 3 Surface excess results for the bulk densities and corresponding pressures with different influence parameters

T^*/T_c^*	Potential	ε_{sf}^*	c_{bulk}^*	p_{bulk}^*	Γ_{const}^*	Γ_{α}^*	Γ_{β}^*
0.8	LJTS 10–4–3	0.3	0.01017	0.008262	0.0062	0.0116	0.0141
			0.01688	0.013171	0.009	0.019	0.028
			0.0226	0.017026	0.011	0.026	0.041
			0.0333	0.023452	0.014	0.039	0.071
			0.04204	0.027973	0.02	0.05	0.10
			0.05075	0.031858	0.018	0.063	0.143
0.8	LJTS 10–4–3	0.514	0.00941	0.007680	0.0129	0.0250	0.0372
			0.01621	0.012700	0.02	0.04	0.07
			0.02157	0.016354	0.0249	0.0548	0.0946
			0.0315	0.022441	0.034	0.079	0.151
			0.03711	0.025502	0.039	0.094	0.188
			0.0419	0.027906	0.04	0.11	0.22
0.8	LJTS 10–4–3	0.75	0.00897	0.007340	0.023	0.045	0.076
			0.01454	0.011507	0.033	0.069	0.116
			0.01887	0.014546	0.042	0.087	0.147
			0.0259	0.019116	0.055	0.116	0.205
			0.0281	0.020455	0.059	0.125	0.224
			0.0298	0.021461	0.062	0.132	0.238
			0.0305	0.021867	0.06	0.14	0.24
			0.0306	0.021925	0.064	0.136	0.245
			0.0317	0.022555	0.07	0.14	0.25
			0.0323	0.022894	0.067	0.143	0.260
0.8	LJTS 10–4–3	2.0	0.00053	0.000456	0.026	0.056	0.089
			0.00242	0.002058	0.065	0.119	0.178
			0.00553	0.004618	0.111	0.183	0.254
			0.01117	0.009021	0.186	0.271	0.355
			0.0156	0.012267	0.249	0.334	0.428
			0.0201	0.015378	0.322	0.402	0.516
			0.0239	0.017861	0.40	0.49	0.59
			0.0273	0.019973	0.487	0.571	0.672
0.8	LJ 10–4–3	0.514	0.00925	0.007556	0.0181	0.0321	0.0472
			0.02095	0.015945	0.038	0.074	0.122
			0.0305	0.021867	0.056	0.113	0.208
			0.037	0.025444	0.071	0.147	0.294
1.1	LJTS 10–4–3	0.514	0.01006	0.011559	0.0087	0.0144	0.0171
			0.03299	0.035254	0.02	0.04	0.06
			0.05053	0.051054	0.026	0.054	0.083
			0.0664	0.063755	0.029	0.066	0.104
			0.08285	0.075452	0.031	0.076	0.121
			0.1062	0.089759	0.03	0.09	0.14
			0.1258	0.099948	0.029	0.092	0.155

Table 3 (continued)

T^*/T_c^*	Potential	ε_{sf}^*	c_{bulk}^*	p_{bulk}^*	Γ_{const}^*	Γ_{α}^*	Γ_{β}^*
			0.1489	0.110164	0.023	0.094	0.166
			0.1698	0.118035	0.01	0.09	0.17
0.8	LJTS 9–3	0.514	0.0097	0.007849	0.0070	0.0125	0.0153
			0.0224	0.016721	0.0133	0.0297	0.0469
			0.03334	0.023252	0.018	0.046	0.083
			0.04654	0.029634	0.022	0.067	0.148
0.8	LJ 9–3	0.514	0.00963	0.007849	0.0103	0.0166	0.0200
			0.02213	0.016721	0.022	0.041	0.062
			0.03294	0.023252	0.033	0.067	0.115
			0.0456	0.029634	0.047	0.107	0.239

Calculated with $\kappa_{const}^* = 2.7334$, $\kappa_{\alpha}^* = -7.5c^{*2} + 11.0c^*$, $\kappa_{\beta}^* = 15.5c^{*2} + c^*$

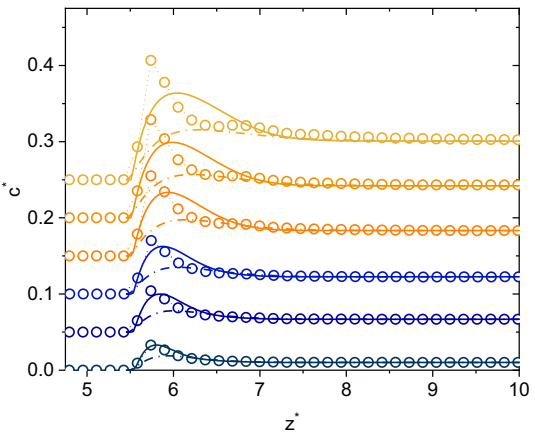

Fig. 12 Density profiles of the adsorption at $T^*/T_c^* = 0.8$, the solid is described by a LJTS potential with $\varepsilon_{sf}^* = 0.3$. The MD data are plotted as circles, with dotted lines as a guide to the eye, the constant influence parameter as dashed line and the density dependent influence parameter set α ($\kappa^* = -7.5c^{*2} + 11.0c^*$) data as line. The bulk densities are 0.01017, 0.01688, 0.0226, 0.0333, 0.04204, 0.05075, and they are shifted by 0.0, 0.05, 0.1, 0.15, 0.2, 0.25, respectively (Color figure online)

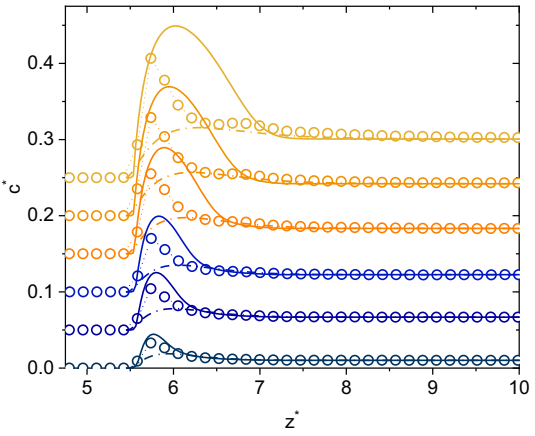

Fig. 13 Density profiles of the adsorption at $T^*/T_c^* = 0.8$, the solid is described by a LJTS potential with $\varepsilon_{sf}^* = 0.3$. The MD data are plotted as circles, with dotted lines as a guide to the eye, the constant influence parameter as dashed line and the density dependent influence parameter set β ($\kappa^* = 15.5c^{*2} + c^*$) data as line. The bulk densities are 0.01017, 0.01688, 0.0226, 0.0333, 0.04204, 0.05075, and they are shifted by 0.0, 0.05, 0.1, 0.15, 0.2, 0.25, respectively (Color figure online)

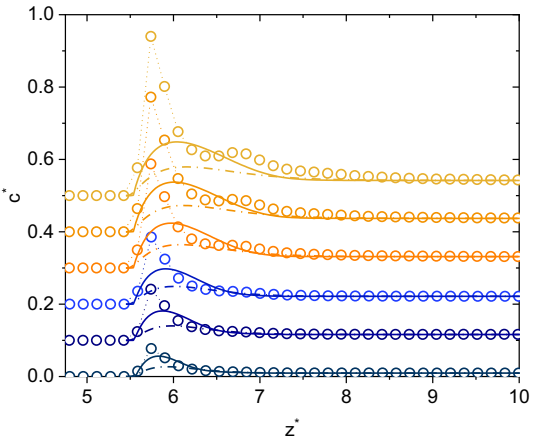

Fig. 14 Density profiles of the adsorption at $T^*/T_c^* = 0.8$, the solid is described by a LJTS potential with $\varepsilon_{sf}^* = 0.514$. The MD data are plotted as circles, with dotted lines as a guide to the eye, the constant influence parameter as dashed line and the density dependent influence parameter set α ($\kappa^* = -7.5c^{*2} + 11c^*$) data as line. The bulk densities are 0.00941, 0.01621, 0.02157, 0.0315, 0.03711, 0.0419, and they are shifted by 0.0, 0.1, 0.2, 0.3, 0.4, 0.5, respectively (Color figure online)

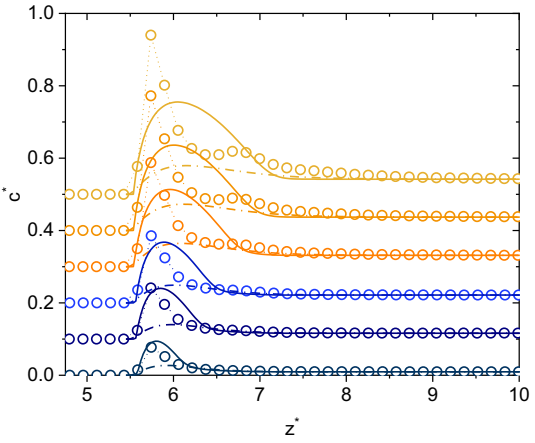

Fig. 15 Density profiles of the adsorption at $T^*/T_c^* = 0.8$, the solid is described by a LJTS potential with $\varepsilon_{sf}^* = 0.514$. The MD data are plotted as circles, with dotted lines as a guide to the eye, the constant influence parameter as dashed line and the density dependent influence parameter set β ($\kappa^* = 15.5c^{*2} + c^*$) data as line. The bulk densities are 0.00941, 0.01621, 0.02157, 0.0315, 0.03711, 0.0419 and they are shifted by 0.0, 0.1, 0.2, 0.3, 0.4, 0.5, respectively (Color figure online)

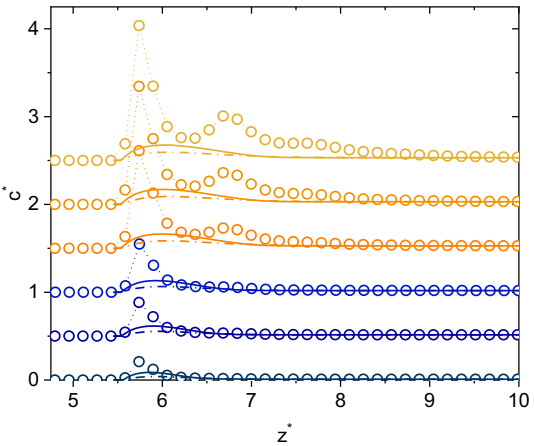

Fig. 16 Density profiles of the adsorption at $T^*/T_c^* = 0.8$, the solid is described by a LJTS potential with $\varepsilon_{sf}^* = 0.75$. The MD data are plotted as circles, with dotted lines as a guide to the eye, the constant influence parameter as dashed line and the density dependent influence parameter set α ($\kappa^* = -7.5c^{*2} + 11c^*$) data as line. The bulk densities are 0.00897, 0.01454, 0.01887, 0.0281, 0.0305, 0.0323, and they are shifted by 0.0, 0.5, 1, 1.5, 2, 2.5, respectively (Color figure online)

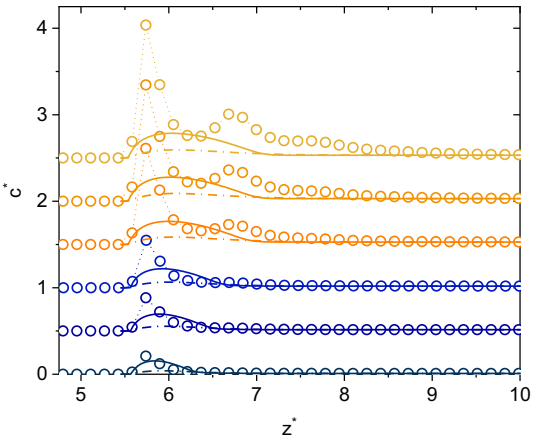

Fig. 17 Density profiles of the adsorption at $T^*/T_c^* = 0.8$, the solid is described by a LJTS potential with $\epsilon_{sf}^* = 0.75$. The MD data are plotted as circles, with dotted lines as a guide to the eye, the constant influence parameter as dashed line and the density dependent influence parameter set β ($\kappa^* = 15.5c^{*2} + c^*$) data as line. The bulk densities are 0.00897, 0.01454, 0.01887, 0.0281, 0.0305, 0.0323, and they are shifted by 0.0, 0.5, 1, 1.5, 2, 2.5, respectively (Color figure online)

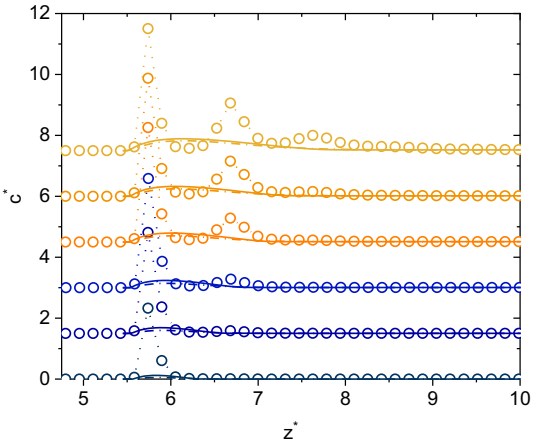

Fig. 18 Density profiles of the adsorption at $T^*/T_c^* = 0.8$, the solid is described by a LJTS potential with $\epsilon_{sf}^* = 2.0$. The MD data are plotted as circles, with dotted lines as a guide to the eye, the constant influence parameter as dashed line and the density dependent influence parameter set α ($\kappa^* = -7.5c^{*2} + 11c^*$) data as line. The bulk densities are 0.00053, 0.00242, 0.00553, 0.01117, 0.0156, 0.0239, and they are shifted by 0.0, 1.5, 3., 4.5, 6, 7.5, respectively (Color figure online)

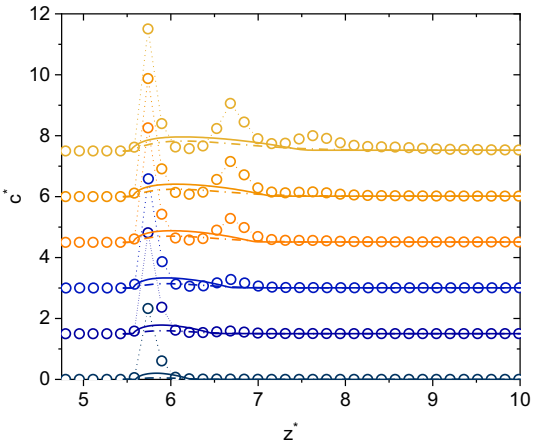

Fig. 19 Density profiles of the adsorption at $T^*/T_c^* = 0.8$, the solid is described by a LJTS potential with $\epsilon_{sf}^* = 2.0$. The MD data are plotted as circles, with dotted lines as a guide to the eye, the constant influence parameter as dashed line and the density dependent influence parameter set β ($\kappa^* = 15.5c^{*2} + c^*$) data as line. The bulk densities are 0.00053, 0.00242, 0.00553, 0.01117, 0.0156, 0.0239, and they are shifted by 0.0, 1.5, 3., 4.5, 6, 7.5, respectively (Color figure online)

shown in Figs. 12 and 13. The parameter set α shows a good description of the MD density profiles, whereas parameter set β overestimates the increase in density close to the surface. At $\varepsilon^*_{sf} = 0.514$, the more satisfying description of the density profiles originates from the parameter set β. At $\varepsilon^*_{sf} = 0.75$ only low bulk densities can be described with the DGT and at $\varepsilon^*_{sf} = 2.0$, the DGT cannot describe surface excess any more, it always underestimates the density profiles.

Acknowledgements The authors acknowledge financial support from the state Tyrol. The computational results presented here have been achieved (in part) using the LEO HPC infrastructure of the University of Innsbruck. We thank Christian Wachsmann and Jana Wolf for valuable discussions.

Author contributions E.M. performed the calculations, prepared the figures and tables, and wrote the manuscript text.K.L. supervised the work scientifically, helped with the code review, and reviewed the manuscript.

Funding Open access funding provided by University of Innsbruck and Medical University of Innsbruck. KL acknowledges funding from the state of Tyrol for the Professorship Thermal Separation Science at University of Innsbruck. No other funding was received for the work in this contribution.

Declarations

Conflict of interest The authors have no competing interests to declare that are relevant to the content of this article.

References

1. C. Tietz, M. Sekulla, X. Yang, R. Schmid, M. Richter, Ind. Eng. Chem. Res. **59**, 13283–13289 (2020). https://doi.org/10.1021/acs.iecr.0c01423
2. M. Richter, M. A. Ben Souissi, R. Span, P. Schley, *J. Chem. Eng. Data* **2014**, *59 (6)*, 2021–2029. DOI: https://doi.org/10.1021/je500181v.
3. C. Wedler, R. Span, Chem. Eng. Sci. **231**, 116281 (2021). https://doi.org/10.1016/j.ces.2020.116281
4. C. Wedler, R. Span, Energy Fuels **35**, 8799–8806 (2021). https://doi.org/10.1021/acs.energyfuels.1c00280
5. T.M. Fieback, R. Span, Energy Procedia **61**, 1501–1504 (2014). https://doi.org/10.1016/j.egypro.2014.12.156
6. P. Chareonsuppanimit, S.A. Mohammad, R.L. Robinson, K.A. Gasem, Int. J. Coal Geol. **95**, 34–46 (2012). https://doi.org/10.1016/j.coal.2012.02.005
7. P. Charoensuppanimit, S.A. Mohammad, K.A.M. Gasem, Energy Fuels **30**, 2309–2319 (2016). https://doi.org/10.1021/acs.energyfuels.5b02751
8. S. Malviya, J.C. Tapia, P. Bai, J. Appl. Phys. (2022). https://doi.org/10.1063/5.0099790
9. E. Sauer, J. Gross, Langmuir **35**, 11690–11701 (2019). https://doi.org/10.1021/acs.langmuir.9b02378

10. J. Liu, L. Wang, S. Xi, D. Asthagiri, W.G. Chapman, Langmuir **33**, 11189–11202 (2017). https://doi.org/10.1021/acs.langmuir.7b02055
11. J. Liu, S. Xi, W.G. Chapman, Langmuir **35**, 8144–8158 (2019). https://doi.org/10.1021/acs.langmuir.9b00410
12. J. Liu, M. Heier, W.G. Chapman, K. Langenbach, J. Chem. Eng. Data **65**, 1222–1233 (2020). https://doi.org/10.1021/acs.jced.9b00585
13. M. Heier, S. Stephan, F. Diewald, R. Müller, K. Langenbach, H. Hasse, Langmuir **37**, 7405–7419 (2021). https://doi.org/10.1021/acs.langmuir.1c00780
14. E.L.C. Vergara, G.M. Kontogeorgis, X. Liang, Ind. Eng. Chem. Res. **58**, 5650–5664 (2019). https://doi.org/10.1021/acs.iecr.9b00137
15. N.J. Corrente, E.L. Hinks, A. Kasera, R. Gough, P.I. Ravikovitch, A.V. Neimark, Carbon **197**, 526–533 (2022). https://doi.org/10.1016/j.carbon.2022.06.071
16. J. Butz, *PhD Thesis,* Karlsruhe Institute of Technology **2019**.
17. C. Miqueu, B. Mendiboure, A. Graciaa, J. Lachaise, Fluid Ph. Equilib. **207**, 225–246 (2003). https://doi.org/10.1016/s0378-3812(03)00028-1
18. P.M.W. Cornelisse, C.J. Peters, J. de Swaan Arons, J. Chem. Phys. **106**, 9820–9834 (1997). https://doi.org/10.1063/1.473872
19. V.G. Baidakov, S.P. Protsenko, G.G. Chernykh, G.S. Boltachev, Phys. Rev. E **65**, 41601 (2002). https://doi.org/10.1103/PhysRevE.65.041601
20. R. Evans, Adv. Phys. **28**, 143–200 (1979). https://doi.org/10.1080/00018737900101365
21. J. Escobedo, G.A. Mansoori, AIChE J. **42**, 1425–1433 (1996). https://doi.org/10.1002/aic.690420523
22. M. Heier, F. Diewald, M.T. Horsch, K. Langenbach, R. Müller, H. Hasse, J. Chem. Eng. Data **64**, 386–394 (2019). https://doi.org/10.1021/acs.jced.8b00927
23. M. Heier, F. Diewald, R. Müller, K. Langenbach, H. Hasse, J. Chem. Eng. Data **66**, 3722–3734 (2021). https://doi.org/10.1021/acs.jced.1c00350
24. S. Stephan, H. Hasse, Phys. Chem. Chem. Phys. **22**, 12544–12564 (2020). https://doi.org/10.1039/d0cp01411g
25. M. Horsch, H. Hasse, ChemBioEng Rev. **2**, 303–310 (2015). https://doi.org/10.1002/cben.201500010
26. H. Zhang, B. Zhang, J. Lu, S. Liang, Chem. Phys. Lett. **366**, 24–27 (2002). https://doi.org/10.1016/S0009-2614(02)01509-9
27. K.S. Walton, D.S. Sholl, AIChE J. **61**, 2757–2762 (2015). https://doi.org/10.1002/aic.14878
28. A. Erto, A. Lancia, D. Musmarra, Microporous Mesoporous Mater. **154**, 45–50 (2012). https://doi.org/10.1016/j.micromeso.2011.10.041
29. J. Wu, AIChE J. **52**, 1169–1193 (2006). https://doi.org/10.1002/aic.10713
30. E. Sauer, J. Gross, Ind. Eng. Chem. Res. **56**, 4119–4135 (2017). https://doi.org/10.1021/acs.iecr.6b04551
31. D. Fu, J.-F. Lu, J.-C. Liu, Y.-G. Li, Chem. Eng. Sci. **56**, 6989–6996 (2001). https://doi.org/10.1016/S0009-2509(01)00331-1
32. J. Gross, J. Chem. Phys. **131**, 204705 (2009). https://doi.org/10.1063/1.3263124
33. S. Enders, K. Quitzsch, Langmuir **14**, 4606–4614 (1998). https://doi.org/10.1021/la9712707
34. H. Kahl, S. Enders, Phys. Chem. Chem. Phys. **4**, 931–936 (2002). https://doi.org/10.1039/b108535m
35. H. Kahl, S. Enders, Fluid Ph. Equilib. **172**, 27–42 (2000). https://doi.org/10.1016/S0378-3812(00)00361-7
36. B. Breure, C.J. Peters, Fluid Ph. Equilib. **334**, 189–196 (2012). https://doi.org/10.1016/j.fluid.2012.08.010
37. X. Liang, M.L. Michelsen, G.M. Kontogeorgis, Fluid Ph. Equilib. **428**, 153–163 (2016). https://doi.org/10.1016/j.fluid.2016.06.017
38. J. Mairhofer, J. Gross, Fluid Ph. Equilib. **439**, 31–42 (2017). https://doi.org/10.1016/j.fluid.2017.02.009
39. C. Miqueu, B. Mendiboure, C. Graciaa, J. Lachaise, Fluid Ph. Equilib. **218**, 189–203 (2004). https://doi.org/10.1016/j.fluid.2003.12.008
40. P. Rehner, J. Gross, Phys. Rev. E (2018). https://doi.org/10.1103/physreve.98.063312
41. S. Stephan, J. Liu, K. Langenbach, W.G. Chapman, H. Hasse, J. Phys. Chem. C **122**, 24705–24715 (2018). https://doi.org/10.1021/acs.jpcc.8b06332

42. S. Stephan, K. Langenbach, H. Hasse, J. Chem. Phys. **150**, 174704 (2019). https://doi.org/10.1063/1.5093603
43. P.M. Larsen, B. Maribo-Mogensen, G.M. Kontogeorgis, Fluid Ph. Equilib. **408**, 170–179 (2016). https://doi.org/10.1016/j.fluid.2015.08.024
44. D. Duque, J.C. Pàmies, L.F. Vega, J. Chem. Phys. **121**, 11395–11401 (2004). https://doi.org/10.1063/1.1818679
45. C.I. Poser, I.C. Sanchez, J. Colloid Interface Sci. **69**, 539–548 (1979). https://doi.org/10.1016/0021-9797(79)90142-5
46. J. Butz, P. Zimmermann, S. Enders, Chem. Eng. Sci. **171**, 513–519 (2017). https://doi.org/10.1016/j.ces.2017.06.019
47. J. Butz, S. Enders, J. Chem. Eng. Data (2023). https://doi.org/10.1021/acs.jced.3c00341
48. J. Vrabec, G.K. Kedia, G. Fuchs, H. Hasse, Mol. Phys. **104**, 1509–1527 (2006). https://doi.org/10.1080/00268970600556774
49. M. Thol, G. Rutkai, R. Span, J. Vrabec, R. Lustig, Int. J. Thermophys. **36**, 25–43 (2015). https://doi.org/10.1007/s10765-014-1764-4
50. M. Heier, S. Stephan, J. Liu, W.G. Chapman, H. Hasse, K. Langenbach, Mol. Phys. **116**, 2083–2094 (2018). https://doi.org/10.1080/00268976.2018.1447153
51. J. Gross, G. Sadowski, Ind. Eng. Chem. Res. **40**, 1244–1260 (2001). https://doi.org/10.1021/ie0003887
52. V. Bongiorno, H.T. Davis, Phys. Rev. A **12**, 2213 (1975)
53. J.D. van der Waals, Z. Phys. Chem. **13U**, 657–725 (1894). https://doi.org/10.1515/zpch-1894-1338
54. J.W. Cahn, J.E. Hilliard, J. Chem. Phys. **28**, 258–267 (1958). https://doi.org/10.1063/1.1744102
55. W.A. Steele, Surf. Sci. **36**, 317–352 (1973). https://doi.org/10.1016/0039-6028(73)90264-1
56. B.S. Carey, L.E. Scriven, H.T. Davis, AIChE J. **26**, 705–711 (1980). https://doi.org/10.1002/aic.690260502
57. B.F. McCoy, H.T. Davis, Phys. Rev. A **20**, 1201–1207 (1979). https://doi.org/10.1103/physreva.20.1201
58. K. Stöbener, P. Klein, S. Reiser, M. Horsch, K.-H. Küfer, H. Hasse, Fluid Ph. Equilib. **373**, 100–108 (2014). https://doi.org/10.1016/j.fluid.2014.04.009
59. M.J.D. Powell, Comput. J. **7**, 155–162 (1964). https://doi.org/10.1093/comjnl/7.2.155